Amorphous saturated Cerium-Tungsten-Titanium oxide nanofibers catalysts for NOx selective catalytic reaction

Dankeaw, Apiwat; Gualandris, Fabrizio; Silva, Rafael Hubert ; Norrman, Kion; Gudik-Sørensen, Mads; Kammer Hansen, Kent; Ksapabutr, Bussarin ; Esposito, Vincenzo; Marani, Debora

Published in:
New Journal of Chemistry

Link to article, DOI:
10.1039/C8NJ00752G

Publication date:
2018

Document Version
Peer reviewed version

NJC

Accepted Manuscript

ROYAL SOCIETY OF CHEMISTRY

rsc.li/njc

View Article Online
DOI: 10.1039/C8NJ00752G

Journal Name

ARTICLE

Amorphous saturated Cerium-Tungsten-Titanium oxide nanofibers catalysts for NO_x selective catalytic reaction

Received 00th January 20xx,
Accepted 00th January 20xx

DOI: 10.1039/x0xx00000x

www.rsc.org/

Apiwat Dankeaw,[a,b] Fabrizio Gualandris[a], Rafael Hubert Silva[a,c], Kion Norrman[a], Mads Gudik-Sørensen[a], Kent Kammer Hansen[a], Bussarin Ksapabutr[b], Vincenzo Esposito[a,*] and Debora Marani[a,d]

Herein for the first time, $Ce_{0.184}W_{0.07}Ti_{0.748}O_{2-\delta}$ nanofibers are prepared by electrospinning to serve as catalyst in the selective catalytic reduction (SCR) process. The addition of cerium is proven to inhibit crystallization of TiO_2, yielding an amorphous TiO_x-based solid solution stable up to 500 °C in air, with supersaturated substitutional Ce. At higher temepratures, anatase phase (titanium oxide) is then observed along with fluorite (cerium oxide). Tungsten is instead demonstrated to promote the reduction of the Ce^{4+} to Ce^{3+} with formation of oxygen vacancies (δ). Catalytic experiments at the best working conditions (dry and in absence of SO_2) are performed to characterize the intrinsic catalytic behavior of the new catalysts. At temeprature lower than 300 °C, superior NO_x conversion properties of the amorphous TiO_x nanofibers over the crystallized TiO_2 (anatase) nanofibers are obsreved and attributed to higher specific surface area (SSA), larger amount of oxygen vacancies, and higher amount of Ce^{3+} over the Ce^{4+}. Comparison with literature data for ceria-tungsten-based nanoperticles also points out higher catalytic performances for the the deveoped nanofibers at the lowest temperatures (< 300°C). This is mainly attributed to the unique nanofibrous morpholgy and to the doping approach. Stability of the amorphous Ce-W-TiO_x nanofibers over time (120 h) and over a number of cycles (5) is demonstrated. Yet, superior catalytic performances of the developed catalysts in a wide range of temperatures (200-500 °C) over state-of-the-art material V-W-titania nanoparticles and nanofibers are also proven.

Introduction

Nitrogen oxides (hereafter NO_x, x = 1, 2), generated from stationary and mobile sources, are recognized as major pollutants responsible for serious damages to the environment and human health [1,2]. The selective catalytic reduction (SCR) of NO_x into harmless products (nitrogen and water) using ammonia as a reducing agent (NH_3-SCR) is a well consolidated technology adopted since the early '80s by both large industrial utilities and automotive players [2-4]. Commercial catalytic systems consist in V_2O_5-WO_3 as active component supported onto anatase phase titanium dioxide (TiO_2) [2-7].

Despite the excellent performances, vanadium-based catalysts also pose severe disadvantages mainly associated with the easy sublimation of V_2O_5 at the typical operation temperatures of a SCR unit, its toxicity, and narrow operation temperature window [6,8-12]. To overcome the mentioned limitations and meet the increasingly stringent regulations about NO_x emissions, several vanadium-free alternative materials have been investigated [6,8-24].

Among others, de-NO_x catalytic properties of cerium-based oxides have been extensively explored due to their excellent oxygen storage and redox (Ce^{4+}/Ce^{3+}) properties that make these materials appropriate candidates either as promotors or as active centres [6,8,19]. A number of studies reports about significant improvements obtained by adding cerium as promoter in low temperature SCR systems such as Mn/TiO_2 [25,26], V-W/TiO_2 [27], Cu/TiO_2 [28], Cu-SAPO-34 monolith catalyst [29]. Yet, when cerium-based materials are used as active catalysts, remarkably high performances have been demonstrated [6,19,20]. In both cases, the improvement can be attributed to an abundance of chemisorbed oxygens, acid sites, and redox shift between (Ce^{4+}/Ce^{3+}) [19]. The addition of a solid acid component as promoter, such as tungsta (WO_3) and niobia (Nb_2O_5), has been proven to further strengthen the SCR activity of ceria-based catalyst by favouring both the reduced state of the active material (Ce^{3+}) and the overall acidity of the catalyst surface [17,19,20]. A number of reports have also pointed out the positive effects of oxygen defects (δ) in $TiO_{2-\delta}$, specifically labile oxygen vacancies (*i.e.* $\delta = [V_O^{\cdot\cdot}]$ in the Kröger-Vink notation) that benefit of relative high mobility [16,19,30,31]. Oxygen

[a] Department of Energy Conversion and Storage, Technical University of Denmark, Frederiksborgvej 399, Roskilde 4000, Denmark.
[b] Department of Materials Science and Engineering, Silpakorn University, Sanamchandra Palace Campus, Nakhon Pathom, 73000, Thailand.
[c] Department of Material, Federal University of Rio Grande do Sul, Av. Osvaldo Aranha 99, Porto Alegre (RS), 90035-190, Brazil.
[d] Centro de Engenharia, Modelagem e Ciências Sociais Aplicadas, Universidade Federal do ABC Av. dos Estados 5001, Santo André (SP), 09210-580, Brazil.
* Corresponding author vies@dtu.dk (Vincenzo Esposito)

View Article Online
DOI: 10.1039/C8NJ00752G

vacancies have been proven to play a crucial role favouring the formation of two Ce^{3+} for each oxygen vacancies, *i.e.* $2Ce'_{Ti} \rightarrow V_O^{\cdot\cdot}$, and the absorption of the SCR reactant species [32]. A synergistic effect between oxygen vacancies, surface acidity and reducibility has been also demonstrated [32]. In this context, the use of amorphous catalysts has been reported to favour the formation of oxygen vacancies, hence to impart superior SCR performance [9,16,19,29,33]. It is also worth mentioning that the amorphous phase is generally regarded as promising substrate for the catalysis as it is considered ideally chemical homogeneous with respect to the related surface properties [34,35].

Besides the tuning of desirable compositions, a further attractive approach adopted to develop catalysts with enhanced properties deals with the control of their morphology [36]. Nanocages, core shell nanoarchitectures, and low dimensional nanostructures (*e.g.* 1D and 2D) have been reported to enhance catalytic performance by enabling an overall increment of the active sites and of their exposure to the reactant species [37-48]. Among others, catalytic nanofibers prepared via electrospinning offer the further advantages of an inexpensive and up-scalable fabrication method together with an easy control over the compositions [41-48]. The resulting nanotextured and widely interconnected open porous network has been proven to enable a fluid dynamic regime favourable for enhanced catalytic activity [41-48].

We here proposed electrospun Ce-W-titania nanofibers as catalyst for the de-NO_x. Compositions at different Ce/W molar ratios were prepared and tested. The compositions at $Ce_{0.184}W_{0.07}Ti_{0.748}O_{2-\delta}$ and $Ce_{0.2}W_{0.2}Ti_{0.6}O_{2-\delta}$ (Ce/W molar ratio of 2:1 and 1:1 respectively) resulted as the best performing catalyst with similar SCR behaviour. In the current manuscript, only the results on the catalyst at lower content of tungsten (Ce/W molar ratio of 2:1) and with a composition fixed at $Ce_{0.184}W_{0.07}Ti_{0.748}O_{2-\delta}$ are discussed.

Experimental

Materials

All materials were reagent grade, used as received, and stored in the desiccator (when required). Titanium tetraisopropoxide (97% purity, Sigma Aldrich, Denmark), tungsten ethoxide (5% w/v in ethanol, Alfa Aesar, Denmark), and cerium (III) nitrate hexa-hydrate (99.5 % purity, Alfa Aesar, Denmark) were used as precursors. Poly (methyl methacrylate) (PMMA; Sigma-Aldrich, Mw ~996,000, Denmark) and glacial acetic acid (99.8%, Sigma Aldrich) were used as carrier polymer and stabilizer for the hydrolysis reaction of the alkoxides, respectively. Ethanol (Anhydrous, 99.9%, Sigma Aldrich, Denmark) was used as solvent.

Preparation of spinning solution

In a typical procedure for the preparation of Ce-W-titania, spinning solutions were prepared by firstly stabilizing the titanium tetraisopropoxide and tungsten ethoxide with acetic acid (*e.g.* molar ratio of acetic acid per the alkoxides was kept at 14.770) under magnetic stirring (20 °C) in a sealed container purged with inert gas (*e.g.* argon) for 15 min. The required amount of the other reagents was then added using adequate syringes. A salt solution of cerium (III) nitrate hexa-hydrate in ethanol at the concentration of 39% w/w was added into the stabilized mixture under mild stirring until a transparent and homogeneous cationic solution at controlled cationic concentration (0.44 mol L^{-1}) was obtained. A PMMA solution (7.5% w/w) was added to adjust the polymer concentration in the spinning solution at 0.56 g L^{-1}. The solution was kept under magnetic stirring for 10 min, and finally loaded in a glass syringe equipped with a 21-gauge stainless steel needle.

Electrospinning of the solution

RT Advanced (Linari Engineering) electrospinning equipment was used. Experimental setup and the conditions used for the preparation of the nanofibers were described elsewhere[44]. The electrospinning process was conducted in air with a voltage supply of 40 kV and a feeding rate of 0.5 ml h^{-1}. The material, resulted in a flexible green mat, was thermally treated in an oven (at different temperature for 3 h, heating rate 5 K min^{-1}) to remove the organics.

Characterization

The thermal properties of the as-prepared nanofibers were investigated (TGA, NETSZCH, STA 409, CD) in air flux from room temperature to 700 °C with a heating rate of 1 K min^{-1}.

BET (Brunauer-Emmett-Teller; Autosorb 1-MP, Quantachrome Instruments, Boynton Beach, Fl, USA) analysis was conducted to measure the specific surface area (SSA) of the materials. Pore volume and pore diameter of the fibrous materials developed were evaluated using Barrett-Joyner-Halenda (BJH) method (AUTOSROB software, AS1WIN).

X-ray diffraction (XRD, Bruker D8, Germany) patterns were recorded at room temperature (Cu Kα radiation) at scanning rate of 0.01 °/s in 2θ range from 10-90°.

The morphology of the nanofibers was analysed by using field emission scanning electron microscopy (FESEM, Supra, Carl Zeiss, Germany) and transmission electron microscopy (TEM, JEM3000F, Oxford Instruments, UK). The chemical composition of the samples was determined by energy-dispersive spectroscopy (EDS) coupled with FESEM.

The oxidation state of the elements involved was investigated using X-ray photoelectron spectroscopy (XPS, K-α, Thermo Electron Limited, Winsford, UK). The analyses were performed as indicated in our previous work[44].

In this paper, catalytic experiments were conducted at dry conditions and in absence of SO_2, especially to characterize the intrinsic catalytic behaviour of the ceria-based catalysts in comparison with that of the state of the art V-W/TiO_2 in the same conditions. The set up for the SCR activity measurements was described elsewhere[44]. 25 mg of catalysts were loaded in the reactor at a total gas flow rate of 6 L h^{-1}. At this weight of

View Article Online
DOI: 10.1039/C8NJ00752G

catalyst, the sample was packed with determined volume to attain the desired GHSV values. The inlet concentrations were: NO = 1,000 ppm, NH_3 = 1,000 ppm, O_2 = 8%, and CO_2 = 5%, with balancing argon gas. During the experiments the temperature was increased stepwise from 100 to 500°C, whereas the NO concentration was continuously monitored by a mass spectrometer (Pfeiffer Vacuum, OmnistraTM GSD 301). The reaction system was maintained for 1 h at each reaction temperature to reach a steady state before performing the analysis of the catalytic performance.

Results and Discussion

In the applied synthesis of the nanofibers, metal oxo/hydroxy polymeric compounds are formed upon hydrolysis-condensation reaction of the precursors metalorganic compounds. At this stage of the processing, the oxides are in an amorphous state characterized by disordered and tiny crystalline clusters, and residual by-products (*e.g.* water, and organics from the synthesis). Purification and crystallization are achieved by low temperatures calcination treatments (300-400 °C) carried out in air to promote oxidation and C-based compound burning [49,50].

The effect of different calcination temperatures on the morphology and crystallographic phase of nanofibers was investigated via thermogravimetry. The conditions for the calcination were fixed based on the results obtained from the thermal analysis. In Figure 1a, the TGA/DTA profiles are reported. The weight loss at temperature lower than 300 °C was associated with the evaporation of the residual solvent from the synthesis. The exothermic process centred at around 300 °C, was ascribed to the completely removal of the organics from the as-prepared nanofibers. At temperatures higher than 300 °C, no weight of loss was identified. In the DTA profile the signal of a second exothermic peak occurring in a range of temperature between 550-600 °C was observed and related to a possible formation of crystallographic (*e.g.* anatase and fluorite) phases. According to these indications, the nanofibers were calcinated at temperature higher than 300 °C.

Figures 1b-d show the SEM micrographs for the nanofibers calcinated at 400, 500, and 600 °C, respectively. For the three different calcinated samples an extended nano-textured morphology with nanofibers displaying high aspect ratios and a narrow diameter distribution is observed. An open and widely interconnected porosity is observed and associated with a large porosity volume. A slight decrease of the average diameters for increasing calcination temperature was also observed (see Table 1) and reasonably explained as an effect of the incipient formation of the crystallographic phase.

In agreement with that, a smooth surface without any observed crystallite grains (see Figure 1b, and 1c) is observed for the nanofibers calcinated at 400 and 500 °C, whilst polycrystalline structure with a rough surface characterizes the nanofibers calcinated at 600 °C (see Figure 1d). The compositions of the calcinated nanofibers were also determined via EDS. For brevity, only the results for the nanofibers calcinated at 400 °C (see inset Figure 1b) are reported. The EDS analysis indicates a molar ratio for Ti/Ce/W (1.0000/0.1822/0.0723) that it is consistent with the molar ratio in the initial precursor solution. The morphology and crystallinity of the nanofibers calcinated at different temperatures were further investigated by transmission electron microscopy (TEM). Figures 2a-c show the TEM micrographs at low (Figures 2 left) and high (Figures 2 centre) magnification for the three samples calcinated at 400, 500, and 600 °C, respectively. Amorphous characteristics for the materials calcinated at 400 and 500 °C, are observed and confirmed by the selected-area-electron diffraction (SAED) (Figures 2 right). In contrast, polycrystalline densely packed structure with crystallites dimension between 5-10 nm is observed for the nanofibers calcinated at 600 °C. The SAED suggests a defined arrangement of the atoms on short range, where the dominant phase is the anatase. Signals associated to the fluorite arrangement of cerium oxide is also observed and confirmed by the HR-TEM image (Figure 2c, center) that shows a well-defined organization of the atoms with fringe spacings of 0.36 nm and 0.31 nm indexed to the (101) plane of the anatase phase and to the (111) plane of the fluorite phase, respectively.

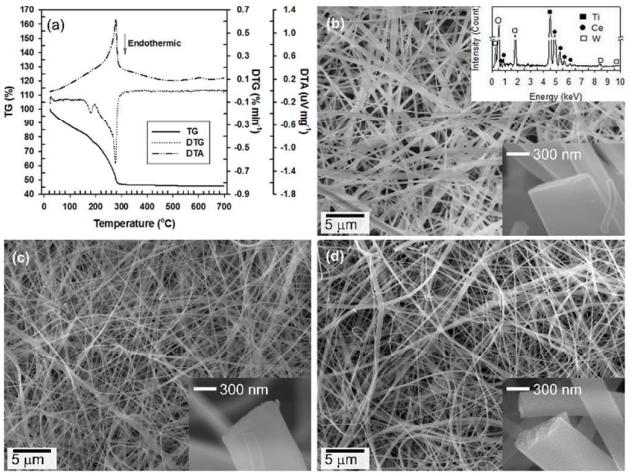

Fig. 1 (a) TG/DTG/DTA curves of as-electrospun nanofibers; SEM micrographs at low and high (insets) magnifications of Ce-W-$TiO_{2-\delta}$ nanofibers calcinated at (b) 400 °C, (c) 500 °C, and (d) 600 °C. The inset in (b) shows the corresponding EDX.

Table 1 Characteristics of nanofibers (phase, diameter, specific surface area, pore diameter, pore volume) calcinated at 400, 500, and 600 °C.

Sample	Phase	Nanofiber average diameter (nm)	Pore diameter (nm)	Specific surface area (m^2/g)
Ce-W-TiO_2@400	Amorphous	231 ± 68	1.90	184
Ce-W-TiO_2@500	Amorphous	215 ± 60	3.47	79
Ce-W-TiO_2@600	Anatase/Fluorite	209 ± 67	7.75	45

View Article Online
DOI: 10.1039/C8NJ00752G

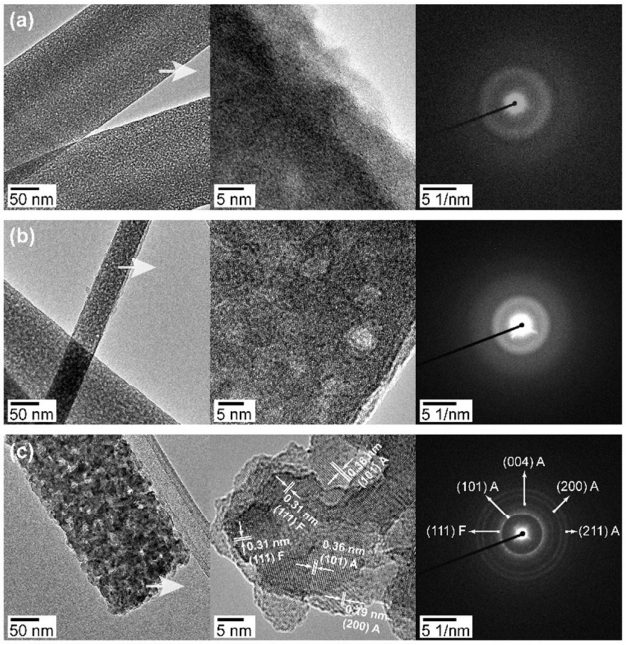

Fig. 2 TEM images of Ce-W-$TiO_{2-\delta}$ nanofibers at low (left) and high (center) magnifications and corresponding selective area electron diffraction (SAED) patterns (right), at different calcination temperatures of (a) 400 °C, (b) 500 °C, and (c) 600 °C. SAEDs were taken from high resolution images (center).

The crystallographic features of the nanofibers were also investigated by XRD macroscopically (see Figure 3a). Anatase phase is assigned both for the pure titania material (calcinated at 400°C) and for the W-titania (calcinated at 400 °C). Given the similar dimension of the two elements (W^{+6} 0.65 Å and Ti^{+4} 0.60 Å in 6-fold coordination), the substitution of Ti^{+4} with W^{+6} into the anatase hosting structure to form a solid solution can be inferred [44]. The alio-valence of the substitutional W, $\boldsymbol{W_{Ti}^{\cdot\cdot}}$, results in double positive charges, that further promotes the oxygen defect annihilation [44]. The presence of the anatase phase also for the W-titania material, supports the hypothesis of the formation of the solid solution. In contrast, no peaks associated with any crystallographic phase are observed for the Ce-titania and for the Ce-W-titania materials calcinated at 400, 450 and 500 °C. In contrast, when temperature reaches the value of 550 °C, a certain degree of order is obtained and the diffraction results in a broad peak, centred in the typical anatase phase pattern. At calcination temperature as high as 600 °C, the co-occurring of the anatase of the titanium oxide and fluorite of the cerium oxide phases can be clearly identified. In agreement with previous literature [51], the influence of Ce addition on the titania crystallization behaviour is observed: TiO_2 crystallization is inhibited by substitutional Ce, amorphous material is thus favoured [51]. Such evidence is also supported by the large mismatch between the ceria and the titania structures. The substitutional Ce^{+4}, although electrostatically neutral with no changes in the oxygen chemistry of the material, *i.e.* $\boldsymbol{Ce_{Ti}^{\times}}$, leads to a large strain due to a large cation mismatch of ca. 45% (Ce^{+4} (0.87 Å) vs Ti^{+4} (0.60 Å) in 6-fold coordination). For the solid solution, a low threshold for substitutional cerium into the anatase hosting structure is thus expected. A low level of saturation for Ce^{3+} in the titania structure, i.e. $\boldsymbol{Ce_{Ti}^{'}}$, is also expected by the even larger dimension of Ce^{+3} (1.01 Å) compared with Ti^{+4} (0.60 Å) in the 6-fold coordination (mismatch above 68 %). Substitutional $\boldsymbol{Ce_{Ti}^{'}}$ also leads to oxygen vacancy formation, i.e. $\boldsymbol{2Ce_{Ti}^{'} \rightarrow V_O^{\cdot\cdot}}$. As conclusive remark, the results suggest the inhibition of the titania crystallization upon cerium addition due to a large strain at lower temperatures (elemental mobility of the diffusive process reduced). Cerium oxide segregation occurs and it is measurable by XRD for an elemental mixture containing 18% molar of Ce. As for the structural features of the nanofibers discussed in Figures 2 and 3, the results suggest that the highly disordered phase from the inorganic polymeric network obtained by sol-gel creates the conditions for a supersaturation of the TiO_2 solution. The thermodynamically stable Ce-saturated TiO_2 anatase phase is crystallized when the elemental diffusion is activated at 550-600 °C.

Characterization of the porous structure along with the surface area of the developed catalysts was carried out by the N_2 adsorption-desorption profiles. In Figure 3b, the N_2 adsorption-desorption curves are shown, while data of pore diameter, and specific surface area (SSA) are listed in Table 1. Different behaviours for the nanofibrous catalysts depending on the calcination temperature is observed. The catalyst calcinated at 400 °C exhibits a I curve type with no hysteresis loop, suggesting a monolayer adsorption-desorption behaviour characterized by a microporosity (micropores diameter < 2nm) [52]. For the nanofibrous catalysts calcinated at 500 and 600 °C a IV curves type with H2 hysteresis loop was observed, indicating the presence of mesoporous structures (mesopores diameter 2-50 nm)[52].

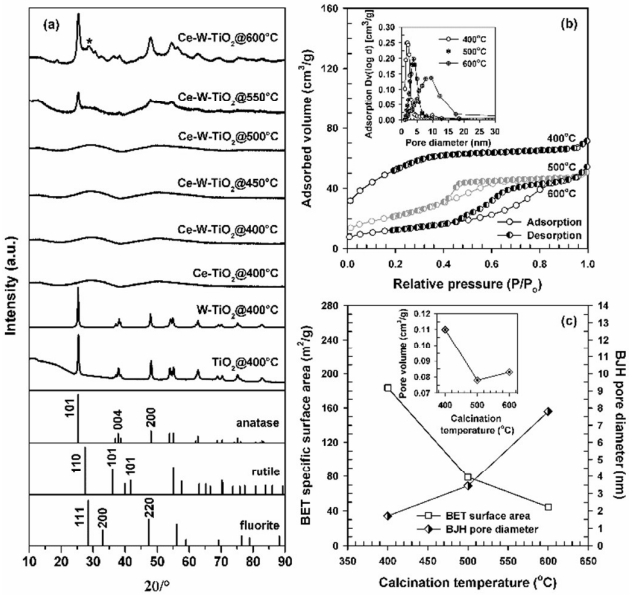

Fig. 3 (a) XRD patterns for the developed nanofibers (The fluorite phase for the cerium oxide is indicated with the star); (b) N_2 adsorption–desorption isotherms and (c) SSA, BJH pore size and pore volume of Ce-W-$TiO_{2-\delta}$ nanofibers calcinated at different temperatures.

View Article Online
DOI: 10.1039/C8NJ00752G

As shown in Figure 3c, both the pore diameter and SSA values significantly vary with the increasing of calcination temperatures. Specifically, the increasing of dimensions of the pore diameter clearly corresponds to a reduction of the SSA values. The incipient crystallization of TiO_2 phase is reasonably responsible for the reduction of the SSA, the increment of the pore diameter, and for the slight contraction of the nanofibers diameter (see Table 1).

The addition of cerium and tungsten is expected to affect electronic structure of titania with a resulting effect on the catalytic properties of the materials. The effect of the two elements on the defect chemistry of the anatase-based nanofibers was explored by the mean of XPS. Figures 4 show the titanium 2p (4a) and oxygen 1s (4b) spectra for the catalysts and for the pure titania. In Figure 4a two peaks corresponding to Ti 2p3/2 and Ti 2p1/2 photo-electron lines for Ti^{4+} are observed for all the samples investigated. Variations in the binding energy from pure titania to the full composition sample is observed and explained as a result of a different electron density around the titanium atoms.

For the W-titania material the observed shift is associated with a greater electronegativity of W (2.36, Pauli scale) compared with titanium (Ti 1.54, Pauli scale). In contrast, for the Ce-titania composition, no significant shift toward the highest energy is observed because of more similar values of electronegativity for the two elements (Ce 1.12 in Pauli scale). In Ce-W-titania catalysts (both the one calcinated at 400 and 600 °C), only a slight shift towards higher binding energy is observed, reasonable associated with the influence of the cerium that attenuates the impact of the tungsten [44].

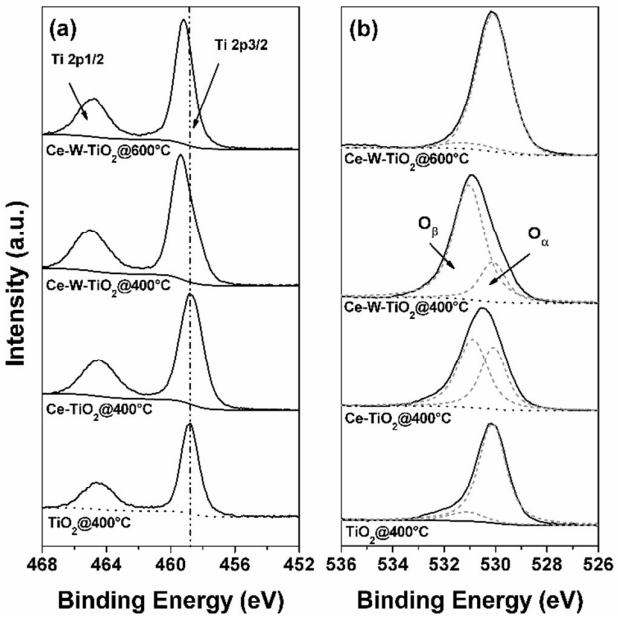

Fig. 4 X-ray photoelectron spectra of (a) Ti2p and (b) O1s for the developed nanofibers.

For all the samples investigated, a wide and asymmetric peak is observed in the O 1s region (Figure 4b), that consists of two distinct bands corresponding to two different chemical states [44]. The signal at low binding energy is assigned to the bulk oxygen bonded either to titanium, whereas the signal at higher energy corresponds to the oxygen defects and chemisorbed oxygen (-OH) [44]. For simplicity, they are referred to as O_α and O_β respectively. Depending on the chemical environment, a variation of the O_β amount is detected and estimated by considering the ratio O_β / (O_α + O_β). The corresponding values are listed in Table 2. In pure titania sample the signal corresponding to the lattice oxygen is the main signal and only a small amount of O_β is observed. Differently, for the Ce-titania amorphous catalyst (calcinated at 400 °C), the amounts of the two oxygen are similar, and for the Ce-W-titania catalyst calcinated at 400 °C, the ratio is reversed with the amount of O_β larger than that one of O_α. This can be ascribed to a larger amount of oxygen defects, specifically $V_O^{\cdot\cdot}$, that characterize the amorphous state of the titania as discussed and reported in literature[53]. When the catalyst is calcinated at 600 °C, the crystallization of the titania is responsible for a lower amount of oxygen defects (vacancies). Interestingly, for this material a lower value of the oxygen ratio with respect to the pure titania material is obtained, likely due to the highest calcination temperature that might be responsible for the decomposition of most of the oxygen chemisorbed groups.

The analysis of 3d cerium spectra (Figure 5a) reveals the coexistence of the Ce^{3+} and Ce^{4+} at a reciprocal ratio that depends on the specific chemical environment. The amount of the two oxidation states for cerium is estimated by the ratio of Ce^{3+}/ (Ce^{3+} + Ce^{4+}). The resulting values are listed in Table 2. The addition of tungsten in the catalyst calcinated at 400 °C with respect to the Ce-titania material, causes an increase on Ce^{3+}. This is explained as a result of the compensation mechanism for the excessive charge introduced by the substitution of Ti^{4+} with W^{6+}. The delocalized extra charge can be either promoted to the conduction bands enhancing the conductivity properties of the materials or transferred to the neighbouring sites promoting their reduction (*e.g.* Ce^{4+}→ Ce^{3+}) [44].

Table 2 $O_\beta/(O_\alpha+O_\beta)$ and $Ce^{3+}/(Ce^{3+} + Ce^{4+})$ ratio for the developed nanofibers materials.

Sample	$O_\beta/ (O_\alpha + O_\beta)$	$Ce^{3+}/ (Ce^{3+} + Ce^{4+})$
TiO_2@400	0.14	/
Ce-TiO_2@400	0.56	0.36
Ce-W-TiO_2@400	0.72	0.46
Ce-W-TiO_2@600	0.05	0.20

View Article Online
DOI: 10.1039/C8NJ00752G

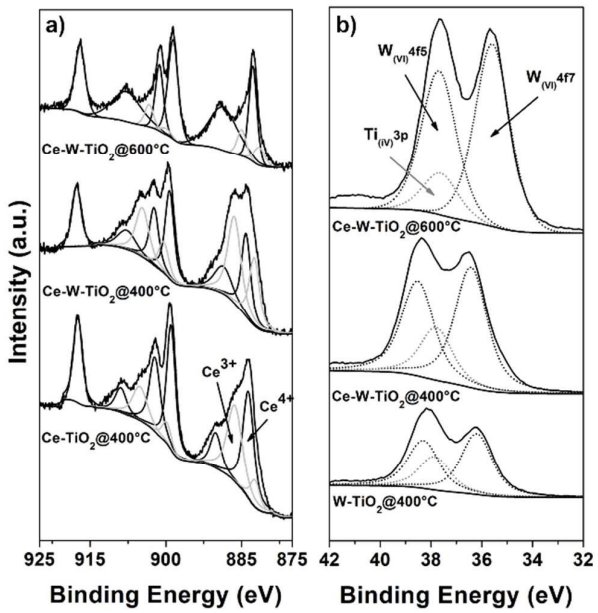

Fig. 5 X-ray photoelectron spectra of (a) W4f and (b) Ce3d for the developed nanofibers.

This latter mechanism is likely responsible for the larger amount of Ce^{3+} in the Ce-W-titania catalyst in the supersaturated materials[44]. It is worth mentioning that the reduction from Ce^{4+} to Ce^{3+} is an energetically convenient process as indicated by the standard reduction potential for the couple Ce^{4+}/Ce^{3+} (E_0= 1.61 V). A higher concentration of Ce^{3+} is expected to enhance the catalytic conversion performances of the ceria-based SCR catalysts [17,19,20,32]. For the full composition catalyst calcinated at 600 °C the ratio is then reduced as a result of the high temperature at the oxidation conditions (calcination in air) that favours the Ce^{4+} state of oxidation [54,55].

The analysis of the tungsten 4f spectra (Figure 5b) excludes the reduction of W^{6+} to W^{5+}, as only signals deriving from W^{6+} can be detected. This result is also supported by the standard reduction potential for the couple W^{6+}/W^{5+} (E_0= -0.03 V).

The morphological and crystallographic features, the oxidation states and the chemistry defects observed for the developed materials provide a set of information for a clear understanding of the catalytic activity. Figures 6 a-d show the NO_x conversion efficiency for the nanofibrous catalysts. Catalytic activity experiments were conducted only in dry conditions and in the absence of SO_2 with the aim of characterizing the intrinsic activity of the materials at the best working conditions.

In addition, the experiments were intentionally conducted on a small amount of materials (25 mg), to appreciate any possible difference at the highest temperatures. Indeed, in a typical experiment conducted on a larger amount of material (*e.g.* 100 mg), when the activation threshold temperature (T_a) for the process is exceeded, NO_x conversion reaches the 100% value. In these conditions, any differences in the conversion behaviour among the samples are not detectable.

In Figure 6a the NO_x conversion values for the full composition catalysts calcinated at different temperatures are plotted as function of temperature. The experiments were conducted at a value of gas hourly space velocity (GHSV) of 400,000 h^{-1}. The catalyst calcinated at 400°C exhibits superior catalytic properties in the low range of temperature, with conversions almost of 50% and 85% at 200 °C and 250 °C, respectively. These values are around 20% higher than the corresponding conversion values of the catalysts calcinated at higher temperatures. The superior performances can be ascribed to a synergism between the high value of SSA and the oxygen vacancies. Interestingly, the material exhibiting the poorest performances is the crystalline catalyst (calcinated at 600 °C). However, when 300 °C is reached and then exceed, no difference among the performances of the catalysts is observed. The conversion values for all the materials are around 90% over a wide range of temperatures, namely from 300 °C to 450 °C. In this region the reaction is likely controlled by transport phenomena of reagents.

The catalytic properties of the best performing catalyst (Ce-W-TiO_2 calcinated at 400 °C) was then explored at different GHSV values (see Figure 6b). As expected, high conversion (~90%) region is obtained at the lowest values of GHSV, and similar behaviour is observed at GHSV values of 200,000 and 400,000 h^{-1}.

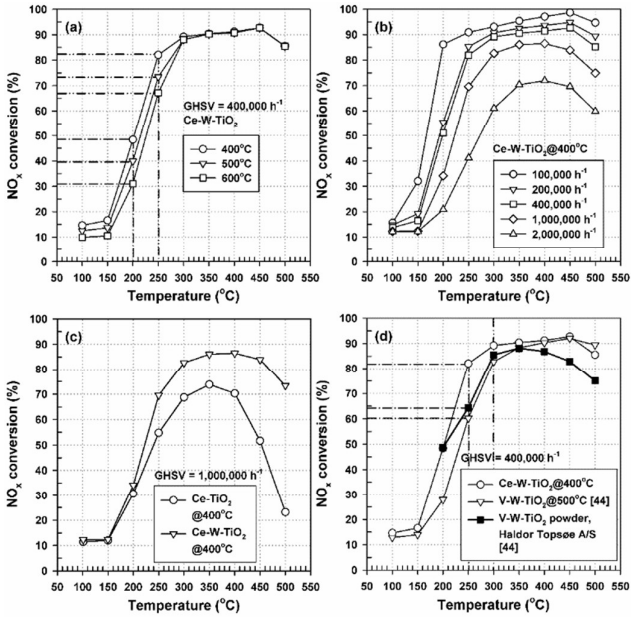

Fig. 6 NO_x conversions of Ce-W-$TiO_{2-\delta}$ nanofibers (a) calcinated at 400, 500, and 600 °C (GHSV of 400,000 h^{-1}); (b) at different GHSVs (nanofibers calcinated at 400 °C); (c) comparison with the ceria-doped catalyst without W-doping (GHSV 1,000,000 h^{-1}) and (d) comparison with the state-of-the-art nanofiber and nanoparticle catalysts from literature [44].

View Article Online
DOI: 10.1039/C8NJ00752G

Remarkably, at 1,000,000 h^{-1}, the catalyst exhibits a conversion higher than 80% in the range of temperatures from 300 °C to 450 °C, whereas when a GHSV of 2,000,000 h^{-1} is used the catalyst can retain a conversion around 70%. These promising results can be ascribed to a number of different factors such as the amorphous state, the extended SSA, the intimate mixing of the elements in the solid solution, and the nanofibrous morphology.

To verify the effect of the W on the catalytic performances, the NO_x conversion properties of the single Ce-titania-based materials were explored and compared with those of the Ce-W-titania catalyst (both calcinated at 400 °C).

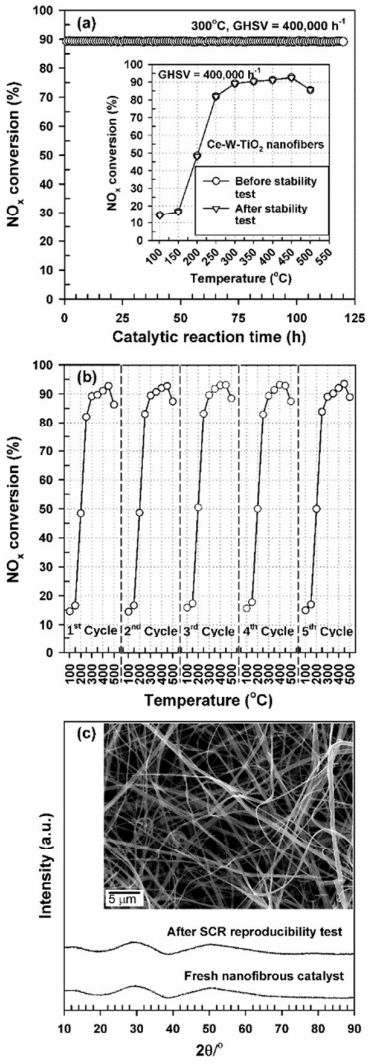

Fig. 7 (a) Long-term stability test (120 h) at 300 °C of the Ce-W-$TiO_{2-\delta}$ catalyst (calcinated at 400 °C); (b) stability of the Ce-W-$TiO_{2-\delta}$ catalyst (calcinated at 400 °C) over 5 working cycles (GHSV of 400,000 h^{-1}); (c) XRD patterns of Ce-W-$TiO_{2-\delta}$ nanofibers (calcinated at 400 °C) before and after NH_3-SCR test, long-term stability, and the 5-cycle stability tests. The inset is a SEM micrograph of nanofibers after the stability tests.

Figure 6c shows the conversion efficiency plots for the Ce and Ce-W-titania materials. The superior performance of the full composition material over the Ce-TiO_2 catalyst is consistent with its higher amount of Ce^{3+}. This result is supported by literature data that indicates the prevail of Ce^{3+} over Ce^{4+} as a factor favouring enhanced catalytic performances [17,19,20,32]. Comparison with the state of the art material (V- W-titania) nanoparticles (catalyst from Haldor Topsoe) and nanofibers (see Figure 6d) from our previous publication [44], suggests superior performances for the Ce-W-titania catalysts at temperatures lower than 300 °C. At a temperature as high as 250 °C, NO_x conversion value for the ceria-based material slightly higher than 80% is observed. When the temperature of 300 °C is exceeded, the performance of the nano-particles powder gradually declines, whilst the nano-fibrous catalysts (both vanadium and cerium-based material) exhibit stable and high level of conversion over a wide range of temperature. At the highest temperature, the nanofibrous morphology is likely the major factor in enhancing the catalytic activity, supporting a favourable fluid-dynamic regime and efficient exposure of the active materials towards the reagents.

In Table 3 a comparison between the NOx conversions of the nanofibrous catalysts reported in the current study, and literature data obtained from nanoparticles ceria-based mixed oxide [24,33,56,57] is indicated. Only the comparison at temperatures lower than 300 °C (150 and 200 °C) is reported, because considered indicative of any relevant difference in the behaviour of the catalysts. At higher temperatures, when the regime working region is reached, the conversion reaction mostly depends on the transport phenomena of reagents[44,48]. In this region of temperatures, the amount of the catalyst used can also influence the values of conversion obtained, likely making the comparison not reliable[44,48].

Interestingly, the developed nanofibrous catalysts exhibit superior NOx conversion performances compared with the literature data. Superior behaviour of the nanofibers is observed despite the marked differences in the experimental conditions, such as for instance the GHSV, and the amount of catalysts used in the experiments. Indeed, conversion values of around 30% and 85% are obtained at 150 °C and 200 °C respectively for the nanofibers at GHSV of 100.000 h^{-1}, whereas at the same temperatures the data from literature indicate conversion values of around 15% and 65% respectively at significantly lower GHSV values (e.g. 25.000 and 90.000 h^{-1}) [24,33,56,57]. The noteworthy high performances of the nanofibers over the nanoparticles can be again ascribed to the unique nanofibrous morphologies that definitely enables an efficient exposure of the active materials towards the flux of the reactants gaseous. In such a morphological configuration, each nanofiber can act as a single nanoreactor assembled with the others into nanostructured, lightweight, and ultra-compact SCR substrate. In addition, the combination of electrospinning and sol-gel approach promotes an optimal level of dispersion of the active materials onto the nano-scaled fibrous titania support. Within this context, it is also worth mentioning that the data from literature corresponds to materials that have been prepared by adopting

View Article Online
DOI: 10.1039/C8NJ00752G

efficient synthetic methods in term of the relevant surface properties of the catalysts [24,33,56,57]. Among others, the homogeneous precipitation is a widely adopted method that enable to design a high level of dispersion of the catalytic materials onto the surface of the titania support. The method enables also a precise control over nanoscale features such as for instance shape and dimensions of the prepared nanostructures[58,59]. Despite these mentioned benefits, the electrospinning/sol-gel proposed approach leads to even higher performances.

At the highest temperatures (> 300 °C), nanofibrous substrate exhibits catalytic performances similar to those that characterize the nanoparticles catalysts.

Table 3 Literature data for Ceria-Tungsten-based mixed oxide catalysts. The compositions are reported indicating the Ce/W molar ratio and considering equal to the unit (1) the molar content of Ti. For each reference only the data of the best performing catalysts are listed.

Comp.	[NH_3] [NO] (ppm)	GHSV (h^{-1})	NOx conv. (%)@150	NOx conv. (%)@200	Reference
$Ce_2W_1O_x$	500	250.000	15	60	[24]
$Ce_1W_1TiO_x$	500	25.000	15	65	[33]
Ce_1W_1TiOx	500	250.000	10	50	[56]
$Ce_3W_1TiO_x$	1000	90.000	10	40	[57]
$Ce_{2.6}W_1TiO_x$	1000	400.000	15	50	Current study
$Ce_{2.6}W_1TiO_x$	1000	100.000	30	85	Current study

The long-term stability of the full composition material (calcinated at 400 °C) was then investigated over a time frame of 120 h. In Figure 7a the NO_x conversion at 300 °C is plotted as function of time. The material exhibits stable and remarkably high de-NO_x conversion value over the entire range of time frame investigated. The NO_x conversion profiles as function of temperature before and after the long-term stability test (inset) are overlapped each other, excluding any either deactivation or degradation process upon the testing treatment. Besides, the stability of the material upon 5 working cycles was also explored (see Figure 7b). Highly reproducible conversion profiles can be observed after any cycle, suggesting again a high stability of the material. Figure 7c shows the XRD patterns for the full composition material before and after the long-term test and the 5 working cycles. None of the tests performed causes crystallization of the nanofibers, as the material clearly retain its amorphous features. In addition, the fibrous morphology (see the inset) is also preserved upon the test treatment.

Conclusions

For the first time, amorphous supersaturated electrospun Ce-W-titanium oxide nanofibers were fabricated via electrospinning process to serve as catalyst for the de-NO_x via NH_3-SCR process. The addition of Ce was proven to inhibit the crystallization of the titania phase, thereby to favor the amorphous state for the catalysts with supersaturated Ce content up to 18% molar. Highly disordered phase from the inorganic polymeric network obtained by sol-gel creates the conditions for the supersaturation of the titania solution, while the thermodynamically stable Ce-saturated TiO_2 anatase phase is crystallized when the elemental diffusion is activated at 500-600 °C. In addition, W was then demonstrated to exert its role by favoring the reduction of Ce^{4+} to Ce^{3+}, thus to enhance the performances of the Ce-W-titania catalyst. NO_x conversion values higher than 90% at GHSV as high as 400,000 h^{-1} were observed in a wide range of temperatures. Remarkably, high conversion values were maintained even at extremely high gas speed (2,000,000 h^{-1}).

At the lowest temperatures (T < 300 °C), the nanofibrous amorphous supersaturated Ce-W-titania material was proven to exhibit superior catalytic performances compared with its corresponding crystalline catalysts, the state-of-the-art material (V-W-titania), and ceria-based nanoparticles (literature data). The further comparison with nanoparticles state-of-the-art catalysts (V-W-titania) indicates also superior performances for the developed Ce-W-titania nanofibrous catalysts. This suggests the nano-fibrous morphology as a crucial factor impacting the NO_x efficiency conversion. The observed key role of the morphology specifically at the lowest temperatures allows indicating the developed nanofibrous ceria-based materials as a catalyst for low temperature range applications.

Besides, highly long-term stability and over multiple working cycles was verified for the developed Ce-W-doped titania nanofibers.

Conflicts of interest

There are no conflicts of interest to declare.

Acknowledgements

Financial support from the Royal Golden Jubilee (RGJ) PhD Program within Thailand Research Fund (TRF), (Contract No.: PHD/0046/2556), is gratefully acknowledged. The authors gratefully acknowledge Dr. Paul Tanchida for the revision of the English in this manuscript.

Notes and references

1 P. Granger, V.I. Parvulescu, *Chem. Rev., 2011,* **111**, 3155-3207.
2 G. Busca, L. Lietti, G. Ramis, F. Berti, *Appl. Catal. B: Environ.*, 1998, **18**, 1-36.

DOI: 10.1039/C8NJ00752G

3 P. Forzatti, I. Nova, E. Tronconi, A. Kustov, J.R. Thøgersenb, *Catal. Today*, 2012, **184**, 153-159.
4 B. Liu, J. Du, X. Lv, Y. Qiu, C. Tao, *Catal. Sci. Technol.*, 2015, **5**, 1241-1250.
5 S.B. Kristensen, A.J. Kunov-Kruse, A. Riisager, S.B. Rasmussen, R. Fehrmann, *J. Catal*., 2011, **284**, 60-67.
6 F. Liu, Y. Yu, H. He, *Chem. Comm.*, 2014, **50**, 8445-8463.
7 G. Dong, Y. Bai, Y.F. Zhang, Y. Zhao, *New J. Chem.*, 2015, **39**, 3588-3596.
8 K. Cheng, J. Liu, T. Zhang, J. Li, Z. Zhao, Y. Wei, G. Jiang, A. Duan, *J. Environ. Sci.*, 2014, **26**, 2106-2113.
9 L. Chen, J. Li, W. Ablikim, J. Wang, H. Chang, L. Ma, J. Xu, M. Ge, H. Arandiyan, *Catal. Lett.*, 2011, **141**, 1859-1864.
10 R. Qu, X. Gao, K. Cen, J. Li, *Appl. Catal. B: Environ.*, 2013, **142-143**, 290-297.
11 W. Shan, F. Liu, H. He, X. Shi, C. Zhang, *Appl. Catal. B: Environ.*, 2012, **115-116**, 100-106.
12 W. Shan, F. Liu, H. He, X. Shi, and C. Zhang, *Catal. Today*, 2012, **184**, 160-165.
13 W. Xu, Y. Yu, C. Zhang, H. He, *Catal. Commun.,* 2008, **9**, 1453-1457.
14 L. Chen, J. Li, M. Ge, and R. Zhu, *Catal. Today*, 2010, **153**, 77-83.
15 X. Gao, Y. Jiang, Y. Fu, Y. Zhong, Z. Luo, K. Cen, *Catal. Commun.*, 2010, **11**, 465-469.
16 P. Li, Y. Xin, Q. Li, Z. Wang, Z. Zhang, L. Zheng, *Environ. Sci. Techn.*, 2012, **46**, 9600-9605.
17 J. Li, G.-Q. Li, Y.-F. Zhang, X.-Q. Liu, Y. Wang, Y. Li, *Appl. Surf. Sci.*, 2017, **401**, 7-16.
18 Y. Peng, K. Li, J. Li, *Appl. Catal. B: Environ.*, 2013, **140–141**, 483-492.
19 L. Yu, Q. Zhong, Z. Deng, S. Zhang, *J. Mol. Catal. A: Chem.*, 2016, **423**, 371-378.
20 K.A. Michalow-Mauke, Y. Lu, K. Kowalski, T. Graule, M. Nachtegaal, O. Kröcher, D. Ferri, *ACS Catal.*, 2015, **5**, 5657-5672.
21 K. Liu, F. Liu, L. Xie, W. Shan, H. He, *Catal. Sci. Techn.*, 2015, **5**, 2290-2299.
22 L. Chen, J. Li, M. Ge, *Environ. Sci. Techn.*, 2010, **44**, 9590-9596.
23 L. Chen, D. Weng, Z. Si, X. Wu, *Progress Natural Sci.: Mater. Intern.*, 2012, **22**, 265-272.
24 W. Shan, F. Liu, H. He, X. Shi, C. Zhang, *Chem. Commun.*, 2011, **47**, 8046-8048.
25 Z. Wu, R. Jin, Y. Liu, H. Wang, *Catal. Commun.*, 2008, **9**, 2217-2220.
26 Z. Wu, R. Jin, H. Wang, Y. Liu, *Catal. Commun.*, 2010, **10**, 935-939.
27 L. Chen, J. Li, M. Ge, *J. Phys. Chem C*, 2009, **113**, 21177-21184.
28 J. Liu, X. Li, Q. Zhao, D. Zhang, P. Ndokoye, *J. Mol. Catal. A: Chem*, 2013, **378**, 115-123.
29 Y. Cao, S. Zou, L. Lan, Z. Yang, H. Xu, T. Lin, M. Gong, Y. Chen, *J. Mol. Catal. A: Chem*, 2015, **398**, 304-311.
30 Z. Deng, Q. Zhong, J. Ding, L. Guo, W. Zhao, S. Zhang, *J Fluorine Chem.*, 2016, **191**, 120-128.
31 J. Ding, Q. Zhong, H. Cai, S. Zhang, *Chem. Eng. J.*, 2016, **286**, 549-559.
32 B. Liu, J. Liu, S. Ma, Z. Zhao, Y. Chen, X.-Q. Gong, W. Song, A. Duan, G. Jiang, *J. Phys. Chem. C,* 2016, **120**, 2271-2283.
33 K. Zhao, W. Han, G. Lu, J. Lu, Z. Tang, X. Zhen, *Appl. Surf. Sci.*, 2016, **379**, 316-322.
34 C. Yoon, D.L. Cocke, *J. Non-Crystalline Solids*, 1986, **79**, 217-245.
35 X. Tang, J. Hao, W. Xu, J. Li, *Catal. Commun.*, 2007, **8**, 329-334.
36 G. Gao, J.-W. Shi, C. Li, C. Gao, Z. Fan, C. Niu, *Appl. Surf. Scie.*, 2017, **411**, 338-346.
37 S. Zhan, M. Qiu, S. Yang, D. Zhu, H. Yu, Y. Li, *J. Mater. Chem. A*, 2014, **2**, 20486-20493.
38 R.-T. Guo, Q.-L. Chen, H.-L. Ding, Q.-S. Wang, W.-G. Pan, N.-Z. Yang, C.-Z. Lu, *Catal. Commun.*, 2015, **69**, 165-169.
39 C. Liu, G. Gao, J.-W. Shi, C. He, G. He, G. Li, N. Bai, C. Niu, *Catal. Commun.*, 2016, **86**, 36-40.
40 H. Jiang, J. Zhao, D. Jiang, M. Zhang, *Catal Lett.* 2014, **144**, 325-332.
41 S. Zhan, J. Yang, Y. Liu, N. Wang, J. Dai, H. Yu, X. Gao, Y. Li, *J. Colloid Interface Sci.*, 2011, **355**, 328-333.
42 B. Li, C. Wang, W. Liu, M. Ye, and N. Wang, *Mater. Letters*, 2013, **90**, 45-48.
43 L. Shahreen, G.G. Chase, A.J. Turinske, S.A. Nelson, N. Stojilovic, *Chem. Eng. J.*, 2013, **225**, 340-349.
44 D. Marani, R. H. Silva, A. Dankeaw, K. Norrman, R. M. Larsen Werchmeister, D. Ippoliti, M. Gudik-Sørensen, K. K. Hansen, V. Esposito, *New J. Chem.*, 2017, **41**, 3466-3472.
45 M.M. Khin, A.S. Nair, V.J. Babu, R. Murugana, S. Ramakrishna, *Energy Environ. Sci.*, 2012, **5**, 8075-8109.
46 X. Chen, P. Wang, P. Fang, H. Eang, C. Cen, W. Zeng, Z. Wu, *Environ. Sci.:* Nano, 2017, **4**, 437-447. 46
47 C. Liu, Q. Ma, H. He, G. He, J. Ma, Y. Liu, Y. Wu, *Environ. Sci.: Nano*, 2017, **4**, 2388-2394.
48 D. Marani, R. H. Silva, A. Dankeaw, M. Gudik-Sørensen, K. Norrman, K. K. Hansen, V. Esposito, *J. Phys. Chem. Solids,* 2018, **118**, 255-261.
49 C. Gadea, D. Marani, V. Esposito, *J. Phys. Chem. Solids*, 2017, **101**, 10-17.
50 C. Gadea, Q. Hnniet, A. Lesch, D. Marani, S.H. Jensen, V. Esposito, *J. Mater. Chem. C*, 2017, **5**, 6021-6029.
51 M. Reli, N. Ambrožova, M. Šihor, L. Matějová, L. Čapek, L. Obalová, Z. Matě, A. Kotarba, K. Koci, *Appl. Catal. B: Environ.*, 2015, **178**, 108-116.
52 M. Kruk, M. Jaronic, *Chem. Mater.*,2001, **13**, 3169-3183.
53 D. Zywitzki, H. Jing, H. Tüysüz, C. K. Chan, *J. Mater. Chem. A*, 2017, **5**, 10957-10967.
54 V. Esposito, D. W. Ni, Z. He, W. Zhang, A. S. Prasad, J. Glasscock, C. Chatzichristodoulou, S. Ramousse, A. Kaiser, *Acta Materialia*, 2013, **61**, 6290-6300.
55 D. Marani, V. Esposito, B.R. Sudireddy, J.J. Bentzen, P.S. Jorgensen, D.W. Ni, F. Teocoli, R. Kiebach, *Ceram. Int.*, 2017, **4**, 5647-5653.
56 W. Shan, F. Liu, H. He, X. Shi, C. Zhang, *Appl. Cat. B: Environ.,* 2012, **115-116**, 100-106.
57 Y. Jiang, Z. Xing, X. Wang, S. Huang, X. Wang, Q. Liu, *Fuel*, 2015, **151**, 124-129.
58 D. Marani, L. P. R. Moraes, F. Gualandris, S. Sanna, D. Z. Florio, V. Esposito, F. C. Fonseca, *CrystEngComm*, 2018, **20**,1405-1410.
59 M. F. S. Machado, L. P. R. Moraes, N. K. Monteiro, V. Esposito, D. Z. de Florio, D. Marani, F. C. Fonseca. *ECS Transaction*, 2017, **78**, 387-394.

View Article Online
DOI: 10.1039/C8NJ00752G

Table of Content Entry

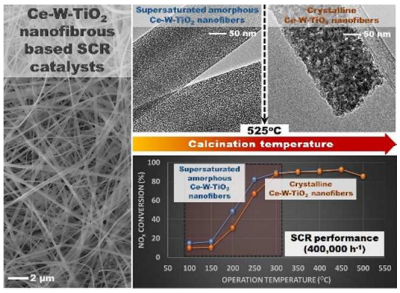

Nano-fibrous, amorphous supersaturated CeO_2/W-TiO_2 SCR catalyst endowed with well-connected and open porosity, high reactivity, and tunable chemistry is herein proposed.